vol. 172, no. 5 the american naturalist november 2008

E-Article

Understanding and Predicting Strain-Specific Patterns of Pathogenesis in the Rodent Malaria *Plasmodium chabaudi*

Nicole Mideo,[1,*] Victoria C. Barclay,[2,†] Brian H. K. Chan,[2,†] Nicholas J. Savill,[2] Andrew F. Read,[2,†] and Troy Day[1,3]

1. Department of Biology, Queen's University, Kingston, Ontario K7L 3N6, Canada;
2. School of Biological Sciences, University of Edinburgh, EH9 3JT Scotland, United Kingdom;
3. Department of Math and Statistics, Queen's University, Kingston, Ontario K7L 3N6, Canada

Submitted February 4, 2008; Accepted May 23, 2008; Electronically published October 3, 2008

abstract: Despite considerable success elucidating important immunological and resource-based mechanisms that control the dynamics of infection in some diseases, little is known about how differences in these mechanisms result in strain differences in patterns of pathogenesis. Using a combination of data and theory, we disentangle the role of ecological factors (e.g., resource abundance) in the dynamics of pathogenesis for the malaria species *Plasmodium chabaudi* in $CD4^+$ T cell–depleted mice. We build a series of nested models to systematically test a number of potential regulatory mechanisms and determine the "best" model using statistical techniques. The best-fit model is further tested using an independent data set from mixed-clone competition experiments. We find that parasites preferentially invade older red blood cells even when they are more fecund in younger reticulocytes and that inoculum size has a strong effect on burst size in reticulocytes. Importantly, the results suggest that strain-specific differences in virulence arise from differences in red blood cell age-specific invasion rates and burst sizes, since these are lower for the less virulent strain, as well as from differences in levels of erythopoesis induced by each strain. Our analyses highlight the importance of model selection and validation for revealing new biological insights.

Keywords: malaria, within-host dynamics, modeling, *Plasmodium chabaudi*, virulence.

* Corresponding author; e-mail: 4nlm@queensu.ca.

† Present address: Center for Infectious Disease Dynamics, Departments of Biology and Entomology, Pennsylvania State University, University Park, Pennsylvania 16802.

Am. Nat. 2008. Vol. 172, pp. E214–E238. 0003-0147/2008/17205-50238$15.00.
DOI: 10.1086/591684

Malaria is one of the leading causes of death among infectious diseases in the world, killing more than one million people every year (WHO and UNICEF 2005). Despite this enormous burden and the large proportion of the world's population that is threatened by malaria, we know little about the relative importance of mechanisms that regulate malaria parasite growth within infected hosts or how differences in these mechanisms among strains give rise to different patterns of morbidity and mortality. A better understanding of these mechanisms is of interest in its own right and will likely yield important insights for improving control strategies and understanding the potential evolutionary consequences of these controls.

The rodent model system of malaria *Plasmodium chabaudi* provides an excellent opportunity to address this question, because controlled and replicated experimental manipulations are possible. In this article, we combine data from experimental manipulations with the development and testing of mathematical models. Our overriding goal is to provide a quantitative (mathematical) description of the main mechanisms governing the regulation of *P. chabaudi* growth within hosts and of how these differ among malaria strains. If a mathematical description cannot be made for mouse models of malaria, where host and parasite genotype together with a vast number of environmental variables can be carefully controlled, then there is little hope for a quantitative understanding of infection in humans.

Many factors regulating malaria infection dynamics have been identified. Among these, immune responses play a large role in the control of parasite densities and may take many forms with respect to the trigger and target of the response (i.e., free-living merozoites or infected red blood cells [RBCs]), the level of clone specificity of the response, and the significance of antigenic variation (for a review, see Stevenson and Riley 2004). Other nonimmunological mechanisms, however, are also likely to play a fundamental role. For example, simple resource abundance—such as the availability of RBCs—is likely a key regulator of parasite growth (Hellriegel 1992; Hetzel and Anderson 1996; Haydon et al. 2003) because it is primarily

within these cells that asexual replication occurs. Also, the age structure of available RBCs could be important (McQueen and McKenzie 2004; Cromer et al. 2006) because many malaria species preferentially invade either young RBCs (reticulocytes) or fully mature normocytes (Paul et al. 2003). Furthermore, the nature of the host's erythropoetic response to malaria-induced anemia will affect both the abundance and age structure of RBCs (Antia et al. 2008), as will temporal patterns of conversion to gametocytes during an infection (e.g., Eichner et al. 2001). Whereas some previous theoretical studies have explored the role of these factors in determining within-host dynamics of malaria, our approach is unique in that we compare multiple model variations that systematically test different combinations of these regulatory mechanisms. Furthermore, we allow for individual variation by fitting models to data sets from individual hosts and then performing a rigorous statistical analysis of the fit to experimental data.

To dissect the relative importance of these factors and how they differ among strains, a combination of experimental manipulation and mathematical modeling is required. Experimental manipulations can be used to remove some potential regulatory mechanisms so that we can examine the dynamics of parasite growth when only a few factors are in operation. In this simplified setting, one can build mathematical models to describe these dynamics. Rigorous tests of these models can then be conducted in this setting through a combination of statistical analyses and further experimental manipulations. Understanding, in a quantitative way, the strain-specific differences that occur in such "stripped-down" situations is an important step toward understanding the more complete picture in which all potential regulatory factors interact with one another.

The results presented here take this approach by focusing on *P. chabaudi* infections in mice that have depleted levels of $CD4^+$ T cells. $CD4^+$ T cells are essential for developing an effective immune response against malaria infections (Good and Doolan 1999; Pombo et al. 2002). They play a crucial role, both early in an infection by activating macrophages and initiating antiparasitic cell-mediated immune responses and in later stages of infection by helping B cells to produce antibodies and in regulating the adaptive immune responses (Langhorne et al. 1990; Urban et al. 2005; Stephens and Langhorne 2006). By removing this regulatory factor, we can then examine the extent to which the above-mentioned ecological factors can explain strain-specific differences in infections.

Material and Methods

Our approach and results have three main components. The first focuses on data from two clones of *Plasmodium chabaudi*, each singly infecting mice that have depleted levels of $CD4^+$ T cells. We build a suite of eight nested models of increasing complexity that represent eight potential descriptions of the within-host dynamics of infection. We then fitted each of these eight models to data using maximum likelihood techniques. Second, we use model selection criteria to choose the "best" model from the eight fitted models for each clone. After statistically determining that the best model does in fact provide a good fit, we use this model to infer the main mechanisms underlying the clone-specific differences in infection dynamics. Third, we take our best model for each clone and use it to derive predictions for the expected dynamics when both clones coinfect a single host. These predictions are compared with experimental data on coinfection as a further independent means of validating the model.

Model Development and Data Fitting

Previous Experimental Data. Experimental infections were generated using two genetically distinct *P. chabaudi* clones, denoted AS and DK, that were originally isolated from thicket rats *Thamnomys rutilans* in the Central African Republic (Beale et al. 1978). In mixed infections, DK is competitively suppressed by AS (Barclay et al. 2008), and previous studies have shown a strong relationship between competitive ability and virulence (de Roode et al. 2003, 2005*a*, 2005*b*; Bell et al. 2006).

Fifteen inbred female C57BL/6JolaHsd mice aged 6–8 weeks (Harlan, Bicester, United Kingdom) were depleted of their $CD4^+$ T cells using a rat monoclonal antibody GK1.5 (for details, see Barclay et al. 2008). Mice were infected via intraperitoneal injection. Five mice were inoculated with 10^5 AS parasites, five received 10^6 of this same clone, and five received 10^6 DK parasites. Mice were maintained as described previously (de Roode et al. 2004). Daily RBC densities were tracked using flow cytometry (Beckman Coulter, High Wycombe, United Kingdom), and parasite densities were measured using a genotype-specific, real-time quantitative polymerase chain reaction (qPCR). One mouse in each of the AS 10^5 and DK 10^6 treatment groups died prematurely; these were therefore excluded from our analysis.

The Model. Our aim is to understand what factors determine the clone-specific differences in dynamics of infection in $CD4^+$ T cell–depleted mice. We developed models that consider clone-specific effects on RBC age structure and cellular tropism, gametocytogenesis, and erythropoesis as possibilities. All of these factors were incorporated in a single large model, and the suite of eight nested models that are the objects of our analysis were then obtained as certain special cases of this single model.

Malaria parasites in most infections display a distinctly discrete replication cycle during an infection, with synchronous bursting of infected RBCs occurring every 24 h in *P. chabaudi* (Carter and Walliker 1975). Our basic model therefore tracks the infection dynamics in discrete time, with one time step corresponding to a single day (Molineaux and Dietz 1999). Immediately after bursting, merozoites begin infecting susceptible RBCs. This process occurs relatively quickly, with the majority of the events during the 24-h period between bursting events consisting of development within RBCs (fig. 1). For simplicity, in the model we census the populations of merozoites and RBCs immediately after bursting but prior to the infection of new RBCs. The basic model thus tracks the following events within a single day: (i) census, (ii) RBC invasion by merozoites, (iii) RBC turnover (production and natural death), and (iv) bursting of infected RBCs (fig. 1).

The discrete-time nature of the model requires that we define distinct classes of RBCs for exploring the importance of RBC age structure to the within-host dynamics. In rats, reticulocytes take 30–75 h to mature when released into the bloodstream, taking longer when the rat is anemic (Ganzoni et al. 1969; Wiczling and Krzyzanski 2007). This time frame is in agreement with the 2–3-day maturation time observed in C57 black mice (S. Reece, personal communication). Because the experimental mice have depressed RBC densities for a substantial duration of the experiment, we assume that the reticulocytes will, on average, take 3 days to mature. Thus, we define four age classes of RBCs: reticulocytes that have been newly introduced to the bloodstream ($R_{1,i}$), reticulocytes in their second day of being in the bloodstream ($R_{2,i}$), reticulocytes in their third day of being in the bloodstream ($R_{3,i}$), and fully mature normocytes (N_i). The subscript i denotes a value on day i after parasite inoculation. In addition to these age classes, there are four classes of infected RBCs corresponding to each type of blood cell ($I_{1,i}$, $I_{2,i}$, $I_{3,i}$, and $I_{N,i}$). Merozoites may infect reticulocytes and normocytes at different per capita rates (reflecting a particular cell age "preference") and may produce different numbers of daughter merozoites per infected cell on bursting. In the absence of evidence to the contrary, merozoites are assumed to respond to all reticulocytes the same way, regardless of how many days the RBC has been in the bloodstream. The production of RBCs varies according to the density of RBCs (i.e., production is increased when an individual becomes anemic), as has been well documented (e.g., Mackey 1997).

Incorporating all of these biological details in a single model gives the discrete-time dynamics system (see app. A for model derivation and table 1 for parameter descriptions):

$$P_{i+1} = \left[\omega_R\left(\sum_{j=1}^{3} R_{j,i}\left\{1 - \exp\left[-\frac{P_i\beta_R}{(R_{1,i} + R_{2,i} + R_{3,i})\beta_R + N_i\beta_N + \mu}\right]\right\}\right) + \omega_N N_i\left\{1 - \exp\left[-\frac{P_i\beta_N}{(R_{1,i} + R_{2,i} + R_{3,i})\beta_R + N_i\beta_N + \mu}\right]\right\}\right] \times (1 - d)(1 - g), \quad (1)$$

$$R_{1,i+1} = \theta[K - (R_{1,i-\tau} + R_{2,i-\tau} + R_{3,i-\tau} + N_{i-\tau})], \quad (2)$$

$$R_{2,i+1} = (1 - d) \times R_{1,i}\exp\left[-\frac{P_i\beta_R}{(R_{1,i} + R_{2,i} + R_{3,i})\beta_R + N_i\beta_N + \mu}\right], \quad (3)$$

$$R_{3,i+1} = (1 - d) \times R_{2,i}\exp\left[-\frac{P_i\beta_R}{(R_{1,i} + R_{2,i} + R_{3,i})\beta_R + N_i\beta_N + \mu}\right], \quad (4)$$

$$N_{i+1} = (1 - d)\left\{R_{3,i}\exp\left[-\frac{P_i\beta_R}{(R_{1,i} + R_{2,i} + R_{3,i})\beta_R + N_i\beta_N + \mu}\right] + N_i\exp\left[-\frac{P_i\beta_N}{(R_{1,i} + R_{2,i} + R_{3,i})\beta_R + N_i\beta_N + \mu}\right]\right\}. \quad (5)$$

We fitted eight variations of this model to the data to determine which factors are important for explaining the dynamics of disease. These eight variations are all special cases of the above general model. Briefly, when there is no age structure, all RBCs (i.e., R_1, R_2, R_3, and N) are collapsed into a single class and there is no heterogeneity in burst size or invasion rate. Constant recovery of RBC deficit means that erythropoesis is a linear function of RBC density (θ is constant under normal conditions and during anemia; $\theta_0 = \theta_A$; see app. A), whereas variable recovery assumes that it is a piecewise linear function ($\theta_0 \neq \theta_A$), which accounts for saturation as described earlier. Gametocyte production, governed by the parameter g, is either assumed not to occur ($g = 0$) or to occur at some constant rate throughout infection. The model variations are as follows (see table C1 for the numbers of fitted parameters). (1) No age structure, constant recovery of RBC deficit (RBC recovery), no gametocyte production (GP); $\beta_R = \beta_N$, $\omega_R = \omega_N$, $\theta_0 = \theta_A$, and $g = 0$. (2) No age structure, constant RBC recovery, constant GP; $\beta_R = \beta_N$, $\omega_R = \omega_N$, and $\theta_0 = \theta_A$. (3) No age structure, variable RBC recovery, no GP; $\beta_R = \beta_N$, $\omega_R = \omega_N$, and $g = 0$. (4) No age structure, variable RBC recovery, constant GP; $\beta_R = \beta_N$ and $\omega_R = \omega_n$. (5) Age structure, constant RBC recovery, no GP; $\theta_0 = \theta_A$ and $g = 0$. (6) Age structure, constant RBC recovery, constant GP; $\theta_0 = \theta_A$. (7) Age structure, variable RBC recovery, no GP; $g = 0$. (8) Age structure, variable RBC recovery, constant GP.

Curve Fitting. Initial conditions for individual mice were

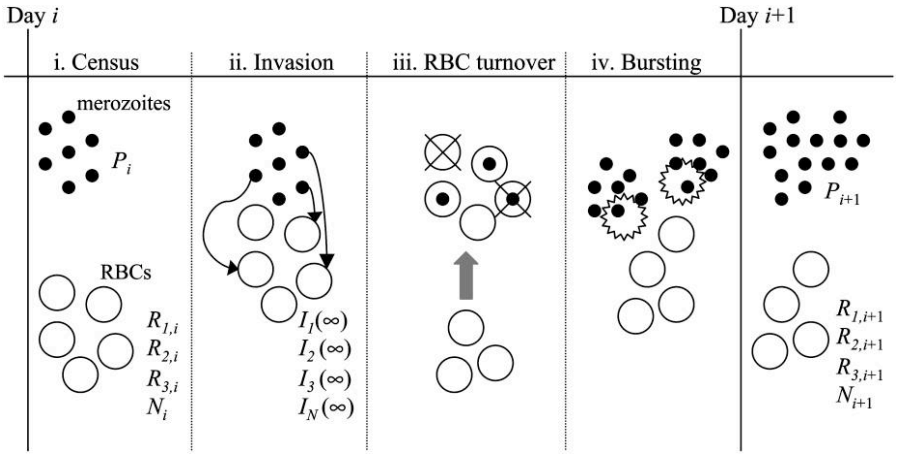

Figure 1: Schematic of asexual blood stage of malaria infections and our model framework. It takes 24 h for *Plasmodium chabaudi* merozoites to invade red blood cells (RBCs), replicate, and burst from infected cells. We model this process in discrete time, tracking the number of merozoites (P_i), reticulocytes of age j ($R_{j,i}$), and normocytes (N_i), on day i. RBC invasion occurs quickly relative to this 1-day cycle. We model this invasion step in continuous time and calculate the number of infected reticulocytes of age j ($I_j(\infty)$) and infected normocytes ($I_N(\infty)$) at the end of this process, when all merozoites are either infecting RBCs or are dead.

determined from experimental measurements of both RBC and parasite densities taken 2 days after inoculation. Parameter estimates were obtained from the literature, and our fitting routine searched a slightly larger parameter space than the biologically reasonable ranges (see table 1). We fitted all parameters except for the merozoite and RBC death rates, which are well known and were fixed for computational practicality (table 1).

The models were fitted to the data from individual mice using the maximum likelihood method. Our approach was to lay a coarse grid over the entire parameter space and, for each parameter set and data point, to calculate the likelihood of the parameters given the data. When the likelihood was maximized over a particular grid, we adjusted the grid using finer-scale steps over a smaller section of parameter space. To find our maximum likelihood parameter estimates, this process was repeated until finer grids failed to achieve a maximum log likelihood greater than that of the previous grid, up to four decimal places. Because we fitted the models to individual mice, we expect the only uncertainties in our data to be caused by measurement error. An earlier experiment estimated the repeatability of RBC densities measured by flow cytometry and parasite densities measured by qPCR. From this we know that the error of the $\log_{10}$-transformed RBC and parasite densities are normally distributed with standard deviations of 0.034 and 0.2, respectively.

Ideally, we would fit the models to both the RBC and the parasite data; however, we have less confidence in our parasite data because of the greater error associated with them. Furthermore, given the discrete-time nature of our model, we can make predictions about the density of merozoites either just after all infected RBCs have burst or just after all merozoites have died or invaded an RBC but before any asexual replication within RBCs has occurred. Our experimental measurements are unlikely to have captured either of these events exclusively, so it is unclear to what we should fit these data. Using only the RBCs to fit the models allows us to avoid this difficulty. Also, because we do not fit our model directly to the parasite data, the parasite density predictions generated from best-fit models provide another qualitative test of the appropriateness of this model. The parasite predictions to which we qualitatively compare our data are those that calculate the density of parasites that have successfully invaded RBCs prior to asexual replication.

With this error structure, the probability of observing 10^D RBCs per μL of blood, given the model that predicts 10^M RBCs per μL of blood, is

$$\Pr(D|M) = \frac{1}{0.034\sqrt{2\pi}}\exp\left[-\frac{(D-M)^2}{2(0.034)^2}\right]. \qquad (6)$$

The likelihood of a particular set of parameters (given the data) is proportional to the product of the probabilities of observing the data (given the model predictions). For numerical accuracy, we take the natural logarithm of the likelihood, so that

$$L = \sum_{q=1}^{t_{max}} \ln\left\{\frac{1}{0.034\sqrt{2\pi}}\exp\left[-\frac{(D_q - M_q)^2}{2(0.034)^2}\right]\right\}, \qquad (7)$$

Table 1: Model parameters, published estimates, and test ranges

Parameter	Definition	Value (range)	Reference
ω_R, ω_N	Mean number of merozoites produced per infected reticulocyte, normocyte	4–10 (2–25)	Garnham 1966; Carter and Walliker 1975; Killick-Kendrick and Peters 1978
β_R, β_N	Invasion rate of reticulocytes, normocytes ($[\text{cells}/\mu\text{L}]^{-1}$ day^{-1})	10^{-6} ($0–2 \times 10^{-5}$)	Hetzel and Anderson 1996[a]; Antia et al. 2008
d	Death rate of RBCs (day^{-1})	.02–.025 (.025)	van Putten 1958[b]; Bannerman 1983
μ	Death rate of merozoites (day^{-1})	40–50 (48)	Garnham 1966; McAlister 1977[a]
g	Proportion of infected RBCs that produce gametocytes	<.1 (0–.5)	Shutler et al. 2005
τ	Lag in RBC production (transit time in bone marrow, days)	2–3 (1–4)	Mary et al. 1980[c]; Chang et al. 2004
θ	Proportion of RBC deficit that is made up each day	.15–.25 (0–1)	Haydon et al. 2003

Note: Unless otherwise noted, estimates are restricted to *Plasmodium chabaudi* and C57 black mice. RBC = red blood cell.

[a] *Plasmodium berghei.*

[b] CBAxC57BL mice.

[c] C3H mice.

where D_q is the $\log_{10}$ of the measured RBC density at time q and M_q is found by simulating the model for a particular data set and taking the $\log_{10}$ of the total density of RBCs (reticulocytes and normocytes) at time q. The best-fit parameters for a given model maximize the log likelihood L.

Statistical Analysis

Model Selection and Goodness of Fit. Given the nested nature of our eight model variations, we use the likelihood ratio test to determine the best-fit model. If the calculated maximum log likelihoods for models A and B are L_A and L_B, respectively, and if model A has fewer fitted parameters, then we define

$$\mathcal{R} = 2(L_B - L_A). \tag{8}$$

If $\mathcal{R}$ is greater than the χ^2 critical value, as determined from a χ^2 distribution with degrees of freedom equal to the difference in fitted parameters between models A and B, then model B is a significantly better fit at the 5% level (e.g., Hilborn and Mangel 1997; Grimshaw et al. 2001; Johnson and Omland 2004). We perform these pairwise model comparisons for each individual mouse to determine the best-fit model. In addition, we reject any models with best-fit parameters that are in strong disagreement with experimentally determined parameter estimates (table 1).

When we choose a best-fit model for each mouse, we test the goodness of fit of the maximum likelihood parameters of this model knowing that, given the data, the likelihood of these parameters is proportional to $L_{\max}$. To perform the goodness-of-fit test, we assume that the model and parameters are true and we simulate 1,000 artificial data sets by generating RBC predictions and incorporating the error structure described in "Curve Fitting." Because we assume that the model is true, any of these artificial data sets could have been the measured one, so we can generate an expected distribution for $L_{\max}$ by calculating the likelihoods of the parameters given these artificial data sets. If the observed $L_{\max}$ lies within the 95% highest-density region of its expected distribution, then the parameters are considered to be a good fit and are accepted at the $\alpha = 5\%$ level.

Parameter Significance and Parameter Error Estimates. To determine whether fitted parameters are significant, we set each parameter in turn to 0, recalculate the maximum likelihood, and compare this maximum likelihood to the original using the likelihood ratio test, as described in "Model Selection and Goodness of Fit." If the likelihood score of the model including the parameter is significantly better than the model with the parameter set to 0, then the parameter is significant at the 5% level.

To approximate the uncertainty in our estimated parameters, we generate a probability distribution for each. We again assume that the best-fit parameters and model are the true ones, and we generate 100 artificial data sets for each mouse. This gives us 100 data sets, each of which could have been the actual measured data set and would have resulted in a slightly different set of maximum likelihood parameter estimates. With each of these synthetic data sets, we redo the parameter-fitting routine using the best-fit model and we use these maximum likelihood estimates to generate a probability distribution for each parameter.

Coinfection Experiments

The above model fitting and statistical analysis provide a rigorous approach for model selection, but all of these

techniques make use of the original data set for which the models were constructed. Another powerful approach to further examine the validity of the model is to test it with an independent data set. For example, if the model is a valid description of the disease dynamics in $CD4^+$ T cell–depleted mice, then it can be used to predict how the dynamics would differ under different conditions. These predictions can then be tested with new experimental data.

We take this approach by using the best-fit models obtained above to make predictions about the disease dynamics that are expected if both clones simultaneously infect a single host. To generate model predictions, we extend the model to allow for two distinct clones (see app. B) and set appropriate parameter values. For clone-specific burst size and invasion rate parameters, we use the median values from the two 10^6 experiments. For the parameters governing RBC production, we use the mean of the medians from the two clones, except for the time lag, which must be an integer and thus was set at 2.

The predictions from our model are then compared with data from an experiment. Specifically, we obtained data from four mice that received the same anti-$CD4^+$ treatment as in the previous experiments, were contemporaneously inoculated with 10^6 AS and 10^6 DK parasites, and survived to day 19 after inoculation. One mouse (mouse 3) died prematurely in this experiment and was therefore excluded from the analysis. Experimental details are given by Barclay et al. (2008).

Results

Model Development and Data Fitting

Maximum log-likelihood values for each model and mouse are reported in table C1. Using the likelihood ratio test, model 7 was chosen as the best fit for 10 of the 13 mice. The three for which model 7 was not the best fit each had model 8 as a best fit but had maximum likelihood estimates of gametocyte conversion rates that are not easily reconciled with published values (AS 10^5 mouse 1, $g = 0.3$; AS 10^5 mouse 3, $g = 0.19$; AS 10^6 mouse 2, $g = 0.197$). Empirical estimates of gametocyte conversion rates are hard to obtain because only the end product of this process can be counted and the immune system may quickly dispose of maturing gametocytes (Taylor and Read 1997). Instead, some studies have measured the daily proportion of total parasites (gametocytes and merozoites) that are gametocytes (Buckling et al. 1999; Shutler et al. 2005). This serves as a reasonable proxy for conversion rate in the absence of evidence of a strong, gametocyte-specific immune response, considering the relatively long life span in the bloodstream of gametocytes compared with merozoites (gametocyte half-life is estimated to be 8 h for males and 16 h for females; Reece et al. 2003). In experimental infections with the *Plasmodium chabaudi* clone DK under normal conditions, gametocytes make up around 1%–2% of all circulating parasites and, even at their maximum density, do not constitute more than 10% (Shutler et al. 2005). Under maximal stimulation, it is possible that conversion rates reach values above 0.1, but there is no empirical evidence of rates this high being maintained for the duration of the acute phase of infection; therefore, we exclude model 8 for these mice. The next best model for each of these three mice was model 7, so we took this as the best-fit model for these mice for the remainder of the analyses. None of our conclusions about inoculum size or clone effects qualitatively changes by choosing model 8 instead.

The best-fit curves for all mice are in good qualitative agreement with measured RBC densities (see fig. 2). From the best-fit model and parameter estimates, we generated predictions for the parasite dynamics; these are shown, along with experimental data, in figure 3. Considering that we did not use these data for fitting, the model does a good job of qualitatively explaining the parasite dynamics, with a few notable exceptions. For mouse 4 from the AS 10^5 experiment, the model predicts unreasonably high parasite densities for the second peak. There is one potential outlier in the RBC measurements for this mouse occurring on day 10 after inoculation. We omitted this data point, refitted the model, and found much more reasonable predictions for the parasite dynamics (as depicted by the blue line in figs. 2, 3). We denote this modified data set with one outlier omitted as mouse 4′. Also, for mouse 2 from the AS 10^6 experiment, the model fails to capture the timing of parasite peaks. In this data set there were no obvious outliers in the RBC measurements, but the RBC dynamics look very different from those of the other mice in this experiment. In particular, RBC density drops about 2 days later than it does in the other mice, despite similar timing in the parasite peaks, and RBC density fails to show any real increase after the second parasite peak. This mouse was excluded from further statistical analysis.

Statistical Analysis

The goodness-of-fit values of model 7 for all mice are given in the legend of figure 2 and are shown graphically in figure C1. The fits were very good for all mice and all parameters were significant for every mouse. Best-fit parameters for model 7 are shown for individual mice in table C2, and boxplots of estimated parameter distributions are shown in figures C2–C4.

Some trends can be seen when comparing estimated values of certain parameters within individuals. In particular, RBC deficits tend to be made up more quickly under

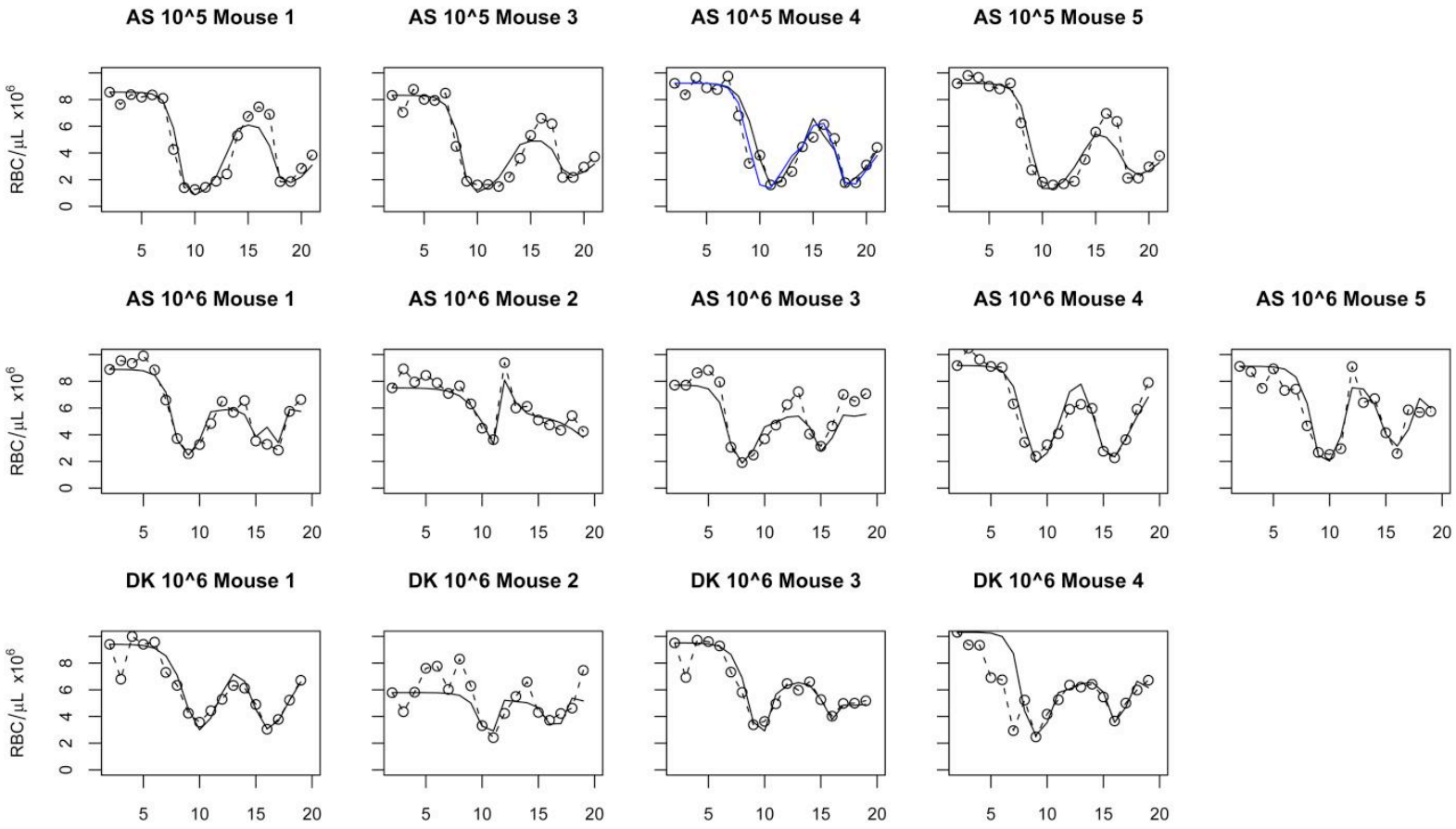

Figure 2: Experimental data and best-fit curves for red blood cell dynamics. *Circles*, observed values; *solid lines*, best fits. Infections are with either 10^5 AS, 10^6 AS, or 10^6 DK parasites. *Blue line*, best-fit curve for mouse 4 in the 10^5 AS experiment with one outlier (day 10) removed (denoted mouse 4′). The fit of the model is very good for all mice. Goodness-of-fit values for the AS 10^5 inoculation: mouse 1 = 388, mouse 3 = 134, mouse 4 = 739, mouse 5 = 134; for the AS 10^6 inoculation: mouse 1 = 824, mouse 3 = 581, mouse 4′ = 590, mouse 5 = 642; for the DK 10^6 inoculation: mouse 1 = 610, mouse 2 = 866, mouse 3 = 727, mouse 4 = 368. Values greater than 50 represent good fits.

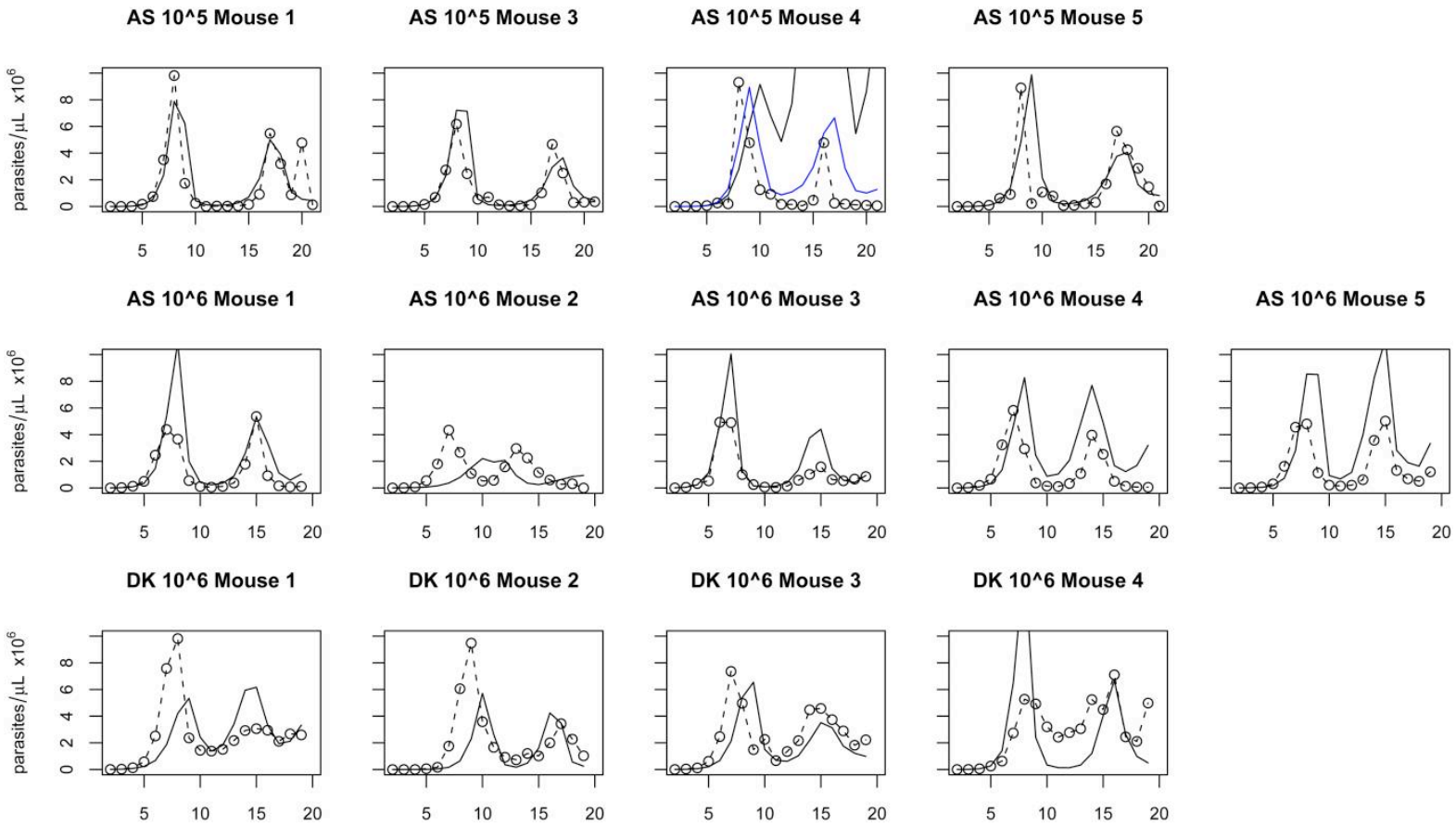

Figure 3: Experimental data and simulations of parasite dynamics. *Circles*, observed values; *solid lines*, model predictions (using parameters fitted to red blood cell data only). Infections are with either 10^5 AS, 10^6 AS, or 10^6 DK parasites. *Blue line*, model predictions for mouse 4 in the 10^5 AS experiment after one outlier (day 10) was removed.

anemic conditions than when RBC densities are normal (i.e., $\theta_0 < \theta_A$; see fig. C4). In addition, one aspect of the importance of RBC age structure is borne out in these distributions: for every individual, the invasion rate of fully mature RBCs is higher than for reticulocytes (i.e., $\beta_R < \beta_N$; see fig. C2), often by an order of magnitude. These invasion rates control for differences in availability, so they truly represent a preference for mature RBCs. Despite this preference, burst size is higher for most individuals in reticulocytes than in normocytes (i.e., $\omega_R > \omega_N$; see fig. C3).

Effect of Parasite Clone. By pooling the data from individuals, we are able to compare the distributions of the parameter estimates to see what effect parasite clone has on the infection dynamics and, in particular, to try to identify the basis for differences in virulence between the DK (less virulent) and AS (more virulent) clones. We compared only those data from inoculations with 10^6 parasites to control for possible inoculum size effects. Boxplots of the pooled distributions are shown in figure C5, and median values are listed in table C3. Table 2 contains estimated DK parameter values relative to the AS values, and we assume, somewhat arbitrarily, that differences of greater than 10% of the AS value are evidence of a clone effect. The median invasion rates of reticulocytes are approximately equal for both clones, but the AS clone has a higher invasion rate of normocytes than the DK clone. Median values for burst size are also higher for the AS parasites than for the DK parasites, and this difference is even more pronounced in reticulocytes than in normocyctes. The mice in the AS-infected group have slower rates of RBC production, both at normal RBC densities and during anemia.

Effect of Inoculum Size. We also compared the distributions of the parameter estimates to see what effect inoculum size has on the infection dynamics. We compared only those data from inoculations with AS parasites to control for possible clone effects. Boxplots of the pooled distributions are shown in figure C6, and median values are listed in table C3. Estimated parameter values for the 10^5 experiment relative to those for the 10^6 experiment are given in table 2. Median values of RBC invasion rate and normocyte burst size are approximately equal. However, there is a marked difference in the median reticulocyte burst sizes, with the low inoculum size obtaining almost twice as many merozites per infected reticulocyte than the high inoculum size. Estimates of RBC production rates are higher in the 10^6 inoculum size than in the 10^5 inoculum size, both at normal RBC densities and during anemia.

Table 2: Medians of pooled estimated parameter distributions relative to AS 10^6 estimated values

Parameter	AS 10^5	AS 10^6	DK 10^6	Inoculum size	Strain
θ_0	.759	1	1.312	X	X
θ_A	.381	1	1.18	X	X
β_R	1.02	1	.940		
β_N	.906	1	.791		X
ω_R	1.943	1	.765	X	X
ω_N	1.002	1	.877		X

Note: We assume that a difference of 10% or greater is evidence of an effect, as indicated by X.

Coinfection Experiments

Model predictions and experimental data from coinfection experiments are plotted in figures 4 and 5. Despite not allowing any individual variation except for starting RBC and parasite densities, the model predictions provide a reasonable qualitative fit to the data, particularly for the early phase of the parasite dynamics. The predicted peaks and troughs in the RBC densities have similar amplitude to the data, but the timing is slightly different. This is especially clear in mice 1 and 2, where RBC densities are predicted to rebound faster than they actually do. This suggests that RBC production in mice with mixed infections is slower than in single-clone-infected mice, since we used the single-clone parameter estimates to generate these predictions. Despite these differences, the parasite density predictions are very good, predicting both the correct timing of peaks and the magnitude of the first wave of parasites. Model predictions and data start to diverge after the first peak, with the model overestimating the level of competitive exclusion of the less virulent DK clone by the relatively more virulent AS clone.

Discussion

We have used a comprehensive combination of mathematical modeling and experimental data to explore the relative importance of ecological factors to the within-host dynamics of *Plasmodium chabaudi* infections. From our best-fit model we conclude that RBC availability is an important regulator of parasite growth in $CD4^+$ T cell–depleted mice, and our systematic approach to model fitting uncovered some of the complexities of this resource and its interaction with the parasite.

Consistent with previous work (Hetzel and Anderson 1996), we find that the loss of RBCs due to infection is sufficient to downregulate parasite densities after the initial peak, and the subsequent increase in RBC production alone generates a second wave of parasites. Recrudescences are conventionally explained as outgrowths by antigenic variants able to escape protective immunity, and it is true

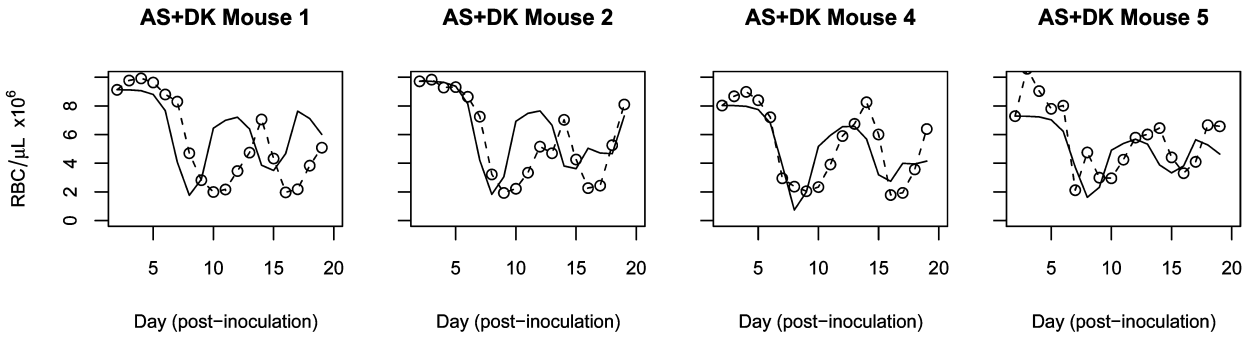

Figure 4: Experimental data and model predictions for red blood cell (RBC) dynamics in competition experiments. *Circles*, observed values; *solid lines*, model predictions. Infections are with 10^6 AS and 10^6 DK parasites; β_R, β_N, ω_R, and ω_N are clone specific and are set to values listed in table C2 for the 10^6 single-clone experiments, and θ_0 and θ_A are set to the mean of the values obtained from these experiments and τ is set to 2, as obtained from the AS 10^6 data.

that recrudescences are antigenically distinct from the primary wave of parasites (Brown and Brown 1965; Phillips et al. 1997). However, because malaria parasites are generating antigenic variation through time, recrudences would be antigenically distinct even if parasite densities were entirely controlled by RBC dynamics. The relative importance of immune evasion and resource limitation remains to be determined in animals with fully intact immune responses.

During periods of anemia, we find that the rate of RBC production is upregulated (similar to findings in Jakeman et al. 1999). Intriguingly, we find that mice infected with the AS clone of *P. chabaudi* have slower rates of RBC production than those inoculated with the DK clone. A similar effect of clone on erythropoesis has been estimated before (Haydon et al. 2003). In our study, it remains unclear whether RBC production is suppressed by the AS clone or enhanced by the DK clone. If future empirical studies can establish a baseline response to anemia, this question could be resolved. Either way, our finding that mice inoculated with the DK clone suffer less anemia may help to explain why the AS clone is relatively more virulent than the DK clone. The details, ubiquity, and adaptive value of this sort of resource manipulation offer many avenues for future investigation.

Recent theory has pointed to a role for RBC age structure in determining relative virulence of *P. chabaudi* clones, with more virulent clones estimated to be able to invade a greater age range of RBCs than less virulent ones (Antia et al. 2008). Our results echo the importance of age structure, but our model takes a different approach and suggests different mechanisms. In particular, Antia et al. (2008) assume that no invasion is possible for RBCs outside a predicted age range and estimate the youngest RBCs each clone is able to infect (8 days for the more virulent clone and 12 days for the less virulent clone). In contrast, we allowed for different invasion rates and burst sizes between types of RBCs and sought to define these types in a biologically meaningful way (i.e., reticulocytes and normocytes). We could then determine whether malaria parasites interact differently with each type of cell and whether these interactions differ between clones.

First, we find that the more virulent clone (AS) has an advantage early on in infections, with a greater invasion rate of and a higher burst size in normocytes than the less virulent clone (DK). Second, although both AS and DK merozoites have lower rates of invasion of reticulocytes, AS gains a fecundity benefit from these invasions, producing more daughter merozoites in younger cells than in fully mature ones. This likely gives AS a big advantage, because RBC production increases when anemia sets in and the system is flushed with reticulocytes. Although no biological mechanism for this higher burst size in reticulocytes is yet known, potential candidates include the fact that the larger size of reticulocytes allows more room for merozoites; that there is a greater structural integrity or deformability of reticulocytes (Taylor-Robinson and Phillips 1994; meaning that older cells may be more rigid and likely to rupture under stress); and, given that reticulocytes are newly introduced into the bloodstream, that their expected circulation time before clearance by the spleen is longer (Loeffler et al. 1989) and the relative risk to the merozoites of undergoing an additional round of asexual multiplication is lower.

In mice with intact immune systems, *P. chabaudi* merozoites infect the most abundant cell type, showing a preference for normocytes early in infections and then switching to reticulocytes when the mouse becomes anemic and the bloodstream flushes with new RBCs (Jarra and Brown 1989; Taylor-Robinson and Phillips 1994). In $CD4^+$ T cell–

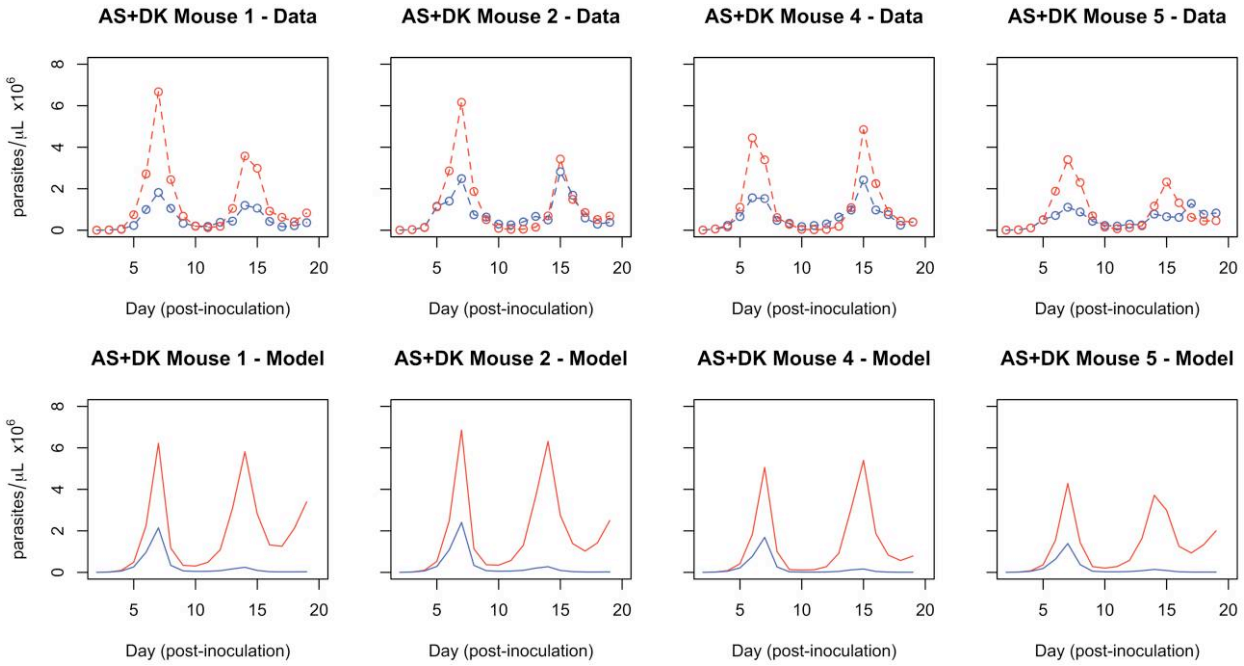

Figure 5: Experimental data and model predictions for parasite dynamics in competition experiments. *Red*, AS parasites; *blue*, DK parasites; *circles*, observed values; *solid lines*, model predictions. Parameters are the same as in figure 4.

depleted mice, infections become chronic, RBC densities remain depressed, and the proportion of circulating reticulocytes remains higher than under normal conditions, although they remain less abundant than mature RBCs (Taylor-Robinson and Phillips 1994). In broad agreement with our "fecundity benefit" hypothesis of reticulocyte invasion, other experimental studies have shown that, in immune-depleted mice, AS parasites continue to show a preference for reticulocytes (Taylor-Robinson and Phillips 1994); that is, they invade reticulocytes more often than would be expected given their relative density. In these mice, the cost of overcoming a lower invasion rate in reticulocytes may be less than the burst size benefit, whereas in the presence of an immune response, the cost of not infecting the most easily accessible cell may be prohibitively high. Predicting a facultative adjustment of a parasite life-history trait in response to the host environment may be novel in the case of RBC preference and host immunity, but it is not unprecedented. Rodent malaria parasites have been shown to alter either their investment in gametocytes or the gametocyte sex ratio in response to host stress (e.g., Buckling et al. 1999; Paul et al. 2003; Reece et al. 2005).

Given this empirical evidence of variable investment in gametocytes throughout infections, and depending on the host environment, modeling conversion rate as a constant throughout the course of infection is inadequate. However, our results suggest that, on average, conversion to gametocytes has no significant effect on the infection dynamics. An alternative approach would be to allow this parameter to vary over time. Although this would perhaps be more biologically realistic, it would also make the parameter fitting process computationally impractical. In its simplest form, our model need not explicitly track gametocytogenesis, as this loss of asexual individuals could be subsumed by the estimates for burst sizes or invasion rates.

Our results present some unexpected differences due to parasite inoculum size. First, inoculum size matters for RBC production, with higher inoculum sizes inducing higher production rates. These parameter estimates are likely due to the fact that, in the experimental data, mice inoculated with 10^5 AS parasites reached lower minimum RBC densities than those who received 10^6 parasites. Greater anemia with a lower inoculum size is not consistent with previous results on inoculum size effects (Timms et al. 2001), although that earlier study was performed in mice with intact immune systems and with different *P. chabaudi* clones. Second, reticulocyte burst sizes are about twofold higher in the 10^5 inoculum size experiment than in the 10^6 inoculum size experiment. One potential explanation of this is the rigidity of the model framework. It could be that, with the larger inoculum size as well as an increased RBC production, the RBCs are maturing

faster so that what we are modeling as reticulocytes are functionally fully mature RBCs; we would then expect the best-fit β_R value to be closer to the β_N value for the 10^6 inoculum size experiment. A more intriguing possibility is that burst size is density dependent, so that the merozoites regulate their usage of RBCs.

We found no consistent estimate of the lag in RBC production from our individual mice. Although published estimates of the transit time of blood cell precursors to the bloodstream tend to be around 3 days (Mary et al. 1980; Chang et al. 2004), this process has been estimated to take as little as 33 h under maximal erythropoetic stimulation (Loeffler et al. 1989). Again, our model did not allow any flexibility in this parameter over time because the discretized description of RBC production meant it had to be an integer. The medians from the pooled distributions do match up with the predictions about RBC production rates: the DK clone induced the highest production rate and had the shortest lag, whereas inoculation with a smaller number of merozoites induced the lowest production rate and had the longest lag. Although the medians from both high-inoculum-size experiments are different, the means were more similar (AS, 2.0 days; DK, 1.7 days) and the true transit time need not be an integer.

Both empirical and theoretical studies have attempted to understand the mechanisms of competition in genetically diverse malaria infections. Experiments with *P. chabaudi* in athymic mice revealed some evidence for immune-mediated apparent competition when the initial wave of parasites receded (Råberg et al. 2006), but when the $CD4^+$ T cell–depleted mice used in the analyses reported here were compared with immune-system-intact control mice, evidence for $CD4^+$ T cell–mediated competition could not be found (Barclay et al. 2008). In the presence of a weak immune response, theory predicts that competition for RBCs is a limiting factor for coinfecting parasites (Hellriegel 1992). Our results confirm this: RBC availability alone can explain the first peak of parasites in $CD4^+$ T cell–depleted mice. The differences in burst sizes and invasion rates of the clones that were derived from our single-strain model generate the appropriate relative heights of the first AS and DK merozoite peaks in coinfections. Beyond the initial peak, our model predictions and the data start to deviate. The model predicts much stronger competitive suppression of the less virulent DK clone by the AS clone than what is seen in the data. Our data are consistent with previous studies in immune-intact mice, which showed that, after the initial peaks, parasite densities were no different or higher in competition than they were in single infections (Bell et al. 2006). The authors of that article point to the immune response becoming more clone specific as an explanation of why the competitively superior clone cannot completely suppress the other. Here, we propose that a similar but $CD4^+$ T cell–independent specific immune response is responsible for the competitive release of the DK clone for which our model could not account. Further insights into the dynamics of coinfections could be found by fitting our competition model to the available data to see whether differences in infection dynamics are solely due to differences in parameters or, alternatively, whether other mechanisms (like our proposed immune response) are in operation.

Although we believe that the ability to predict the outcome of the acute phase of competition experiments provides strong validation of our model, it could be further tested in a number of ways. One option is to empirically test our parameter estimates, although our results show that there will be substantial variation between individual mice. Another option is to experiment with other clones to see whether their relative virulence can be explained by the mechanisms we have proposed. It would also be interesting to see whether there was more evidence of density-dependent regulation of RBC usage and burst sizes, perhaps through experimental manipulation of RBC availability.

The results presented here take a significant first step toward a comprehensive model of the within-host dynamics of malaria infections. We have shown that ecological factors are crucial for explaining infection dynamics and, with this foundation, we can build up the complexity toward a better understanding of the dynamics in the more biologically interesting setting of immune-intact hosts.

Acknowledgments

We thank S. Reece for inspired discussions about the contents of this manuscript and S. Alizon and A. Hurford for comments on earlier drafts. This research was funded by the Wellcome Trust, the Natural Sciences and Engineering Research Council of Canada, and the Canada Research Chairs Program.

APPENDIX A

Model Derivation

The basic structure of the discrete-time model in tracking merozoite density and RBC density is derived by considering the series of events occurring during a single day. Suppose the number of merozoites and susceptible RBCs of each age class per microliter of blood at the census point on day i are given by P_i, $R_{1,i}$, $R_{2,i}$, $R_{3,i}$, and N_i. The next event in the replication cycle is the invasion of susceptible RBCs. We model this as a continuous time process that occurs quickly, relative to the 24 h discrete-time burst cycle. Free-living merozoites invade reticulocytes and normocytes at rates β_R and β_N, respectively, and experience a natural mortality rate μ while in the bloodstream. We assume that merozoites can infect both susceptible and already infected RBCs, but for simplicity (and similar to Hetzel and Anderson 1996) we assume that secondary invasions are lost and do not change the behavior of the primary invasion. Given these assumptions, we can write differential equations to describe the invasion phase. For $j = 1, 2$, and 3 (i.e., the day after the release of the reticulocyte in the bloodstream),

$$\frac{dP}{dt} = -P\left[\beta_R \sum_{j=1}^{3} (R_j + I_j) + \beta_N(N + I_N)\right] - \mu P, \tag{A1}$$

$$\frac{dR_j}{dt} = -\beta_R P R_j, \tag{A2}$$

$$\frac{dN}{dt} = -\beta_N P N, \tag{A3}$$

$$\frac{dI_j}{dt} = \beta_R P R_j, \tag{A4}$$

$$\frac{dI_N}{dt} = \beta_N P N. \tag{A5}$$

Pay special attention to the notation in equations (A1)–(A5). The variables in these equations are missing the subscript i referring to the day in question because these are, in fact, different variables than the P_i, $R_{j,i}$, N_i, $I_{j,i}$, and $I_{N,i}$ introduced above. The variables in equations (A1)–(A5) track the dynamics of the different kinds of cells during the RBC invasion phase only, which occurs as one of the events during each day. The variables subscripted with an i, however, track these values from one day to the next. Thus, the initial conditions for the above system of differential equations on day i are $P(0) = P_i$, $R_j(0) = R_{j,i}$, $N(0) = N_i$, $I_j(0) = 0$, and $I_N(0) = 0$. The solution to this system is readily found, allowing us to calculate the number of each type of cell after this invasion phase is complete; that is, $R_j(\infty)$, $N(\infty)$, $I_j(\infty)$, and $I_N(\infty)$ (note that $P(\infty) = 0$).

The next event is RBC turnover through death and erythropoesis. We suppose that a fraction d of all RBCs die, then RBC aging occurs, and then finally newly produced RBCs enter the age 1 class at a rate that depends on the RBC density τ days earlier. Specifically, we model RBC production in a density-dependent fashion as in Haydon et al. (2003) but with a time lag of τ days between the onset of anemia and the body's response. This represents the time it takes for new blood cells to develop in the bone marrow before being released into the bloodstream. Thus, the number of susceptible age 1 RBCs produced on day i is $\theta[K - (R_{1,i-\tau} + R_{2,i-\tau} + R_{3,i-\tau} + N_{i-\tau})]$, where K represents the equilibrium density of RBCs in the absence of both merozoites and natural death and θ is the proportion of the RBC deficit that is made up in one day. Other forms of RBC production, such as a saturating Hill function, have been suggested (Mackey 1997), but we use this linear form of density dependence for simplicity and we account for a type of saturation of production by having two separate values of θ: one for when RBC level is above 50% of its normal density (θ_0) and another for when it is below 50% (θ_A). We have performed all of the analyses below with a Hill function as well, and this tended to result in qualitatively reasonable but statistically poorer fits to the data (N. Mideo, unpublished results). Last, with the above assumptions, the number of susceptible RBCs of age 2 and age 3 on day i becomes $(R_{1,i} - I_1(\infty))(1 - d)$ and $(R_{2,i} - I_2(\infty))(1 - d)$, respectively, and the number of normocytes becomes $(R_{3,i} - I_3(\infty) + N_i - I_N(\infty))(1 - d)$.

The final event is the bursting of RBCs and the resulting production of merozoites, at which point a new census

occurs. Using ω_R and ω_N as the burst size of infected retoculocytes and normocytes, respectively, the total number of merozoites produced on day i is then $[\omega_R \sum_{j=1}^{3} I_j(\infty) + \omega_N I_N(\infty)](1 - d)(1 - g)$, where g is the proportion of infected RBCs that produce gametocytes rather than merozoites (referred to as the conversion rate). Thus, the discrete time system of equations from one day to the next is

$$P_{i+1} = \left(\omega_R \sum_{j=1}^{3} I_j(\infty) + \omega_N I_N(\infty)\right)(1 - d)(1 - g), \tag{A6}$$

$$R_{1,i+1} = \theta[K - (R_{1,i-\tau} + R_{2,i-\tau} + R_{3,i-\tau} + N_{i-\tau})], \tag{A7}$$

$$R_{2,i+1} = (R_{1,i} - I_1(\infty))(1 - d), \tag{A8}$$

$$R_{3,i+1} = (R_{2,i} - I_2(\infty))(1 - d), \tag{A9}$$

$$N_{i+1} = (R_{3,i} - I_3(\infty) + N_i - I_N(\infty))(1 - d). \tag{A10}$$

Finally, we derive explicit expressions for the number of each type of RBC invaded in a particular cycle by finding general solutions to the differential equations (A1)–(A5). Because the number of total RBCs (uninfected plus infected) remains constant during a bout of invasion (because RBC production and natural death occur in the next step of the discrete cycle), the parasite dynamics do not depend on the dynamics of either. Using this fact and the initial conditions $R_j(0) = R_{j,i}$, $N(0) = N_i$, $P(0) = P_i$, $I_j(0) = 0$, and $I_N(0) = 0$, we can first find an expression for $P(t)$ by solving equation (A1). This gives us

$$P(t) = P_i \exp\{-t[(R_{1,i} + R_{2,i} + R_{3,i})\beta_R + N_i\beta_N + \mu]\}. \tag{A11}$$

Substituting this into equations (A4) and (A5) we find

$$I_j(t) = R_{j,i}\left\{1 - \exp\left[-\frac{(1 - \exp\{-t[(R_{1,i} + R_{2,i} + R_{3,i})\beta_R + N_i\beta_N + \mu]\})P_i\beta_R}{(R_{1,i} + R_{2,i} + R_{3,i})\beta_R + N_i\beta_N + \mu}\right]\right\} \tag{A12}$$

for $j = 1, 2$, and 3, and

$$I_N(t) = N_i\left\{1 - \exp\left[-\frac{(1 - \exp\{-t[(R_{1,i} + R_{2,i} + R_{3,i})\beta_R + N_i\beta_N + \mu]\})P_i\beta_N}{(R_{1,i} + R_{2,i} + R_{3,i})\beta_R + N_i\beta_N + \mu}\right]\right\}. \tag{A13}$$

Further simplification of these expressions is possible because, given our parameters, the number of parasites declines to 0 within a single day. This makes biological sense, because free-living parasites have only a matter of minutes to infect a RBC before they will die naturally. Thus, it is a reasonable approximation to assume that the numbers of infected cells just before bursting are given by the limits of equations (A12) and (A13) as t goes to infinity. Thus,

$$I_j(\infty) = R_{j,i}\left\{1 - \exp\left[-\frac{P_i\beta_R}{(R_{1,i} + R_{2,i} + R_{3,i})\beta_R + N_i\beta_N + \mu}\right]\right\}, \tag{A14}$$

$$I_N(\infty) = N_i\left\{1 - \exp\left[-\frac{P_i\beta_N}{(R_{1,i} + R_{2,i} + R_{3,i})\beta_R + N_i\beta_N + \mu}\right]\right\}. \tag{A15}$$

Substituting the solutions for $I_j(\infty)$ and $I_N(\infty)$ into the above discrete time system, equations (A6)–(A10), gives the complete model of the main text.

APPENDIX B

Competition Model with Two Clones

We can extend our original discrete time framework (eqq. [A6]–[A10]) to allow for two different clones of a parasite, P_A and P_B. Densities of reticulocytes (on their jth day in the bloodstream) and normocytes infected with parasite A are given by I_{jA} and I_{NA}. Reticulocytes and normocytes infected with parasite B are given by I_{jB} and I_{NB}. As before, we assume that only the first parasite to infect an RBC matters. Subsequent invasions are essentially lost, so we have to consider only singly infected RBCs. The basic model tracking parasite and RBC densities is given by:

$$P_{A,i+1} = \left[\omega_{RA}\sum_{j=1}^{3} I_{jA}(P_{A,i}, R_{j,i}) + \omega_N I_{NA}(P_{A,i}, N_i)\right](1-d)(1-g), \tag{B1}$$

$$P_{B,i+1} = \left[\omega_{RB}\sum_{j=1}^{3} I_{jB}(P_{B,i}, R_{j,i}) + \omega_N I_{NB}(P_{B,i}, N_i)\right](1-d)(1-g), \tag{B2}$$

$$R_{1,i+1} = \theta[K - (R_{1,i-\tau} + R_{2,i-\tau} + R_{3,i-\tau} + N_{i-\tau})], \tag{B3}$$

$$R_{2,i+1} = [R_{1,i} - I_{1A}(P_{A,i}, R_{1,i}) - I_{1B}(P_{B,i}, R_{1,i})](1-d), \tag{B4}$$

$$R_{3,i+1} = [R_{2,i} - I_{2A}(P_{A,i}, R_{2,i}) - I_{2B}(P_{B,i}, R_{2,i})](1-d), \tag{B5}$$

$$\begin{aligned} N_{i+1} = {} & [R_{3,i} - I_{3A}(P_{A,i}, R_{3,i}) - I_{3B}(P_{B,i}, R_{3,i})](1-d) \\ & + [N_i - I_{NA}(P_{A,i}, N_i) - I_{NB}(P_{B,i}, N_i)](1-d). \end{aligned} \tag{B6}$$

The dynamics of the invasion phase are now described by the following set of differential equations:

$$\frac{dP_A}{dt} = -P_A\left[\beta_{RA}\sum_{j=1}^{3}(R_j + I_{jA} + I_{jB}) + \beta_{NA}(N + I_{NA} + I_{NB})\right] - \mu P_A, \tag{B7}$$

$$\frac{dP_B}{dt} = -P_B\left[\beta_{RB}\sum_{j=1}^{3}(R_j + I_{jA} + I_{jB}) + \beta_{NB}(N + I_{NA} + I_{NB})\right] - \mu P_B, \tag{B8}$$

$$\frac{dR_j}{dt} = -\beta_{RA}P_A R_j - \beta_{RB}P_B R_j, \tag{B9}$$

$$\frac{dN}{dt} = -\beta_{NA}P_A N - \beta_{NB}P_B N, \tag{B10}$$

$$\frac{dI_{jA}}{dt} = \beta_{RA}P_A R_j, \tag{B11}$$

$$\frac{dI_{NA}}{dt} = \beta_{NA}P_A N, \tag{B12}$$

$$\frac{dI_{jB}}{dt} = \beta_{RB}P_B R_j, \tag{B13}$$

$$\frac{dI_{NB}}{dt} = \beta_{NB}P_B N. \tag{B14}$$

As before, we can find expressions for $P_A(t)$ and $P_B(t)$. These expressions are equivalent to equation (A11), except with strain-specific invasion rates. Given the initial conditions $R_k(0) = R_{k,i}$, $N(0) = N_i$, $P_A(0) = P_{A,i}$, $P_B(0) = P_{B,i}$, $I_{jA}(0) = 0$, $I_{jB}(0) = 0$, $I_{NA}(0) = 0$, and $I_{NB}(0) = 0$,

$$P_A(t) = P_{A,i}\exp\{-t[(R_{1,i} + R_{2,i} + R_{3,i})\beta_{RA} + N_i\beta_{NA} + \mu]\}, \tag{B15}$$

$$P_B(t) = P_{B,i}\exp\{-t[(R_{1,i} + R_{2,i} + R_{3,i})\beta_{RB} + N_i\beta_{NB} + \mu]\}. \tag{B16}$$

Substituting these results into equations (B9) and (B10), we can find expressions for the $R_j(t)$ values and for $N(t)$. Letting $Y_i = R_{1,i} + R_{2,i} + R_{3,i}$,

$$R_j(t) = R_{j,i}\exp\left(-\frac{\{1-\exp[-t(N_i\beta_{NA} + Y_i\beta_{RA} + \mu)]\}P_{A,i}\beta_{RA}}{N_i\beta_{NA} + Y_i\beta_{RA} + \mu}\right.$$

$$\left.-\frac{\{1-\exp[-t(N_i\beta_{NB} + Y_i\beta_{RB} + \mu)]\}P_{B,i}\beta_{RB}}{N_i\beta_{NB} + Y_i\beta_{RB} + \mu}\right), \tag{B17}$$

$$N(t) = N_i\exp\left(-\frac{\{1-\exp[-t(N_i\beta_{NA} + Y_i\beta_{RA} + \mu)]\}P_{A,i}\beta_{NA}}{N_i\beta_{NA} + Y_i\beta_{RA} + \mu}\right.$$

$$\left.-\frac{\{1-\exp[-t(N_i\beta_{NB} + Y_i\beta_{RB} + \mu)]\}P_{B,i}\beta_{NB}}{N_i\beta_{NB} + Y_i\beta_{RB} + \mu}\right). \tag{B18}$$

To a good approximation,

$$\exp[-t(N_i\beta_{NA} + Y_i\beta_{RA} + \mu)] \approx \exp[-t(N_i\beta_{NB} + Y_i\beta_{RB} + \mu)], \tag{B19}$$

which allows us to solve for the numbers of different kinds of infected cells just before bursting. As earlier, we take the limits as t goes to infinity. Thus,

$$I_{jA}(\infty) = \frac{P_{A,i}R_{j,i}\beta_{RA}(N_i\beta_{NB} + Y_i\beta_{RB} + \mu)\left\{1-\exp\left[-\left(\frac{P_{A,i}\beta_{RA}}{Y_i\beta_{RA} + N_i\beta_{NA} + \mu} + \frac{P_{B,i}\beta_{RB}}{Y_i\beta_{RB} + N_i\beta_{NB} + \mu}\right)\right]\right\}}{N_i(P_{A,i}\beta_{RA}\beta_{NB} + P_{B,i}\beta_{RB}\beta_{NA}) + P_{B,i}\beta_{RB}(Y_i\beta_{RA} + \mu) + P_{A,i}\beta_{RA}(Y_i\beta_{RB} + \mu)}, \tag{B20}$$

$$I_{NA}(\infty) = \frac{P_{A,i}N_i\beta_{NA}(N_i\beta_{NB} + Y_i\beta_{RB} + \mu)\left\{1-\exp\left[-\left(\frac{P_{A,i}\beta_{NA}}{Y_i\beta_{RA} + N_i\beta_{NA} + \mu} + \frac{P_{B,i}\beta_{NB}}{Y_i\beta_{RB} + N_i\beta_{NB} + \mu}\right)\right]\right\}}{N_i(P_{A,i} + P_{B,i})\beta_{NA}\beta_{NB} + P_{B,i}(Y_i\beta_{RA} + \mu) + P_{A,i}\beta_{NA}(Y_i\beta_{RB} + \mu)}, \tag{B21}$$

$$I_{jB}(\infty) = \frac{P_{B,i}R_{j,i}\beta_{RB}(N_i\beta_{NA} + Y_i\beta_{RA} + \mu)\left\{1-\exp\left[-\left(\frac{P_{A,i}\beta_{RA}}{Y_i\beta_{RA} + N_i\beta_{NA} + \mu} + \frac{P_{B,i}\beta_{RB}}{Y_i\beta_{RB} + N_i\beta_{NB} + \mu}\right)\right]\right\}}{N_i(P_{A,i}\beta_{RA}\beta_{NB} + P_{B,i}\beta_{RB}\beta_{NA}) + P_{B,i}\beta_{RB}(Y_i\beta_{RA} + \mu) + P_{A,i}\beta_{RA}(Y_i\beta_{RB} + \mu)}, \tag{B22}$$

$$I_{NB}(\infty) = \frac{P_{B,i}N_i\beta_{NB}(N_i\beta_{NA} + Y_i\beta_{RA} + \mu)\left\{1-\exp\left[-\left(\frac{P_{A,i}\beta_{NA}}{Y_i\beta_{RA} + N_i\beta_{NA} + \mu} + \frac{P_{B,i}\beta_{NB}}{Y_i\beta_{RB} + N_i\beta_{NB} + \mu}\right)\right]\right\}}{N_i(P_{A,i} + P_{B,i})\beta_{NA}\beta_{NB} + P_{B,i}(Y_i\beta_{RA} + \mu) + P_{A,i}\beta_{NA}(Y_i\beta_{RB} + \mu)}. \tag{B23}$$

APPENDIX C

Supplementary Results

We use the maximum likelihood method of fitting our model variations to the individual mouse data. Details of the methodology are presented in the main text. The best-fit parameters for a given model maximize the log likelihood L; the maximum likelihood values are presented in table C1. We use the likelihood ratio test to compare the fit of our nested model variations.

As described in "Model Development and Data Fitting," we reject model 8 as the best fit for the three mice data sets that chose this model on the basis of the estimated gametocyte conversion rate g. Thus, the best-fit model for each mouse is model 7 and the best-fit parameters for each individual are given in table C2.

We test the goodness-of-fit of the maximum likelihood parameters of model 7 to the data sets of each individual mouse. The likelihood of these parameters, given the data, is proportional to L_{max}. For this test, we assume that the model and parameters are true and simulate 1,000 artificial data sets by generating RBC predictions and incorporating the error structure described in "Curve Fitting." Each of these data sets represents one that could have been the measured one; we can generate an expected distribution for L_{max} by calculating the likelihoods of the parameters given these artificial data sets. If the observed L_{max} value lies within the 95% highest-density region (HDR) of its expected distribution, then the parameters are considered to be a good fit and are accepted at the $\alpha = 5\%$ level. In figure C1, we plot these distributions and highlight the location of the observed L_{max} within the 95% HDR. The fit is good for each mouse.

We can use the approach described above for generating artificial data sets to approximate the uncertainty in our estimated parameters. We generate 100 artificial data sets for each mouse, each of which again could have been the measured one and would have resulted in a slightly different set of maximum likelihood parameter estimates. With each of these synthetic data sets, we perform the parameter-fitting routine again using the best-fit model, and we use these maximum likelihood estimates to generate a probability distribution for each parameter. These distributions are shown in figures C2–C4.

By pooling the individual probability distributions for each parameter according to experiment (i.e., AS 10^5, AS 10^6, or DK 10^6), we attempt to identify any effects of parasite clone or inoculum size. Median parameter values, according to treatment, are presented in table C3 and are shown graphically, along with distributions, in figures C5 and C6.

Table C1: Maximum log likelihoods (L_{max}) for each model and the best-fit model, as chosen by the likelihood ratio test, for each mouse.

Treatment, mouse	Model (no. parameters)								Best-fit model
	1 (4)	2 (5)	3 (5)	4 (6)	5 (6)	6 (7)	7 (7)	8 (8)	
AS 10^5:									
1	−252.0354	−254.2259	−198.3124	−188.9497	−71.9943	−60.4726	−29.2523	−16.5551	8
3	−145.7672	−148.5523	−102.6568	−99.7949	−74.8265	−58.1948	−33.6190	−31.6321	8
4	−41.778	−41.3139	−34.0503	−33.1802	−32.7567	−31.4321	−15.2876	−17.1742	7
5	−91.2966	−97.2707	−68.2014	−73.0514	−65.1489	−65.4983	−30.5617	−30.1121	7
AS 10^6:									
1	−95.3124	−95.3124	2.5347	3.3676	8.1647	8.1713	21.1703	20.1022	7
2	−28.5043	−28.1106	−17.2592	−20.8733	−15.0168	−13.7768	28.2615	25.6421	8
3	−205.2719	−205.2719	−82.4215	−81.7086	−21.2089	−19.6881	2.6447	3.8579	7
4	−101.6202	−101.6202	−61.5321	−56.9027	2.4884	3.0744	14.3611	14.3611	7
5	−87.6311	−88.0733	−33.816	−33.816	−6.2623	−6.2629	.7489	.276	7
DK 10^6:									
1	5.1129	5.376	20.2243	19.9075	22.3498	23.4571	24.9077	25.5997	7
2	−113.2633	−113.261	−96.7325	−96.7376	−93.2548	−93.25448	−22.9551	−22.9441	7
3	−32.8633	−32.9051	−7.8646	−7.7993	5.5394	8.3251	24.2722	24.3229	7
4	−260.4084	−259.8688	−130.6609	−128.4231	−133.3927	−120.12560	−86.8485	−87.2826	7

Note: Models that share the same number of fitted parameters can be compared directly; that is, a model with a larger L_{max} value is significantly better. For models that differ by one fitted parameter, twice the difference in L_{max} values must be greater than 3.84 for a more complex model to provide a significantly better fit. See "Statistical Analysis" for details.

Table C2: Estimated parameter values for the best-fit model

Treatment, mouse	θ_0	θ_A	$\beta_R \times 10^6$	$\beta_N \times 10^6$	ω_R	ω_N	τ
AS 10^5:							
1	.06901	.18889	1.0889	7.08999	13.8193	9.1826	3
3	.05124	.128	.3918	15.06	21	6.072	3
4	.83897	.5099	9.997	.9889	11.995	22	2
5	.05181	.1309	.7839	12.0610	19.890	6.030	2
AS 10^6:							
1	.04942	.41099	1.0009	16.28	4.649	6.001	3
2	.01877	.5	.589	1.489	2	13.889	1
3	.07664	.5	.2263	12.206	10.999	7.732	3
4	.5	.3715	.8309	3.5002	19	11.021	1
5	.0875	.4491	.843	11.749	15.89	6	2
DK 10^6:							
1	.5	.4389	.8508	4.104	18	7.111	1
2	.04139	.5	.2759	19.825	11.799	5.991	1
3	.1739	.5	.725	7.499	9.46	6.014	1
4	.04983	.3889	.889	10.3891	2.98	8.078	3

Table C3: Medians of pooled estimated parameter distributions

Parameter	AS 10^5	AS 10^6	DK 10^6
θ_0	.0759	.10	.1312
θ_A	.1999	.52509	.6196
β_R	1.086×10^{-6}	1.065×10^{-6}	1.001×10^{-6}
β_N	10.14×10^{-6}	11.189×10^{-6}	8.861×10^{-6}
ω_R	15.778	8.12	6.21
ω_N	7.998	7.979	7.0
τ	3	2	1

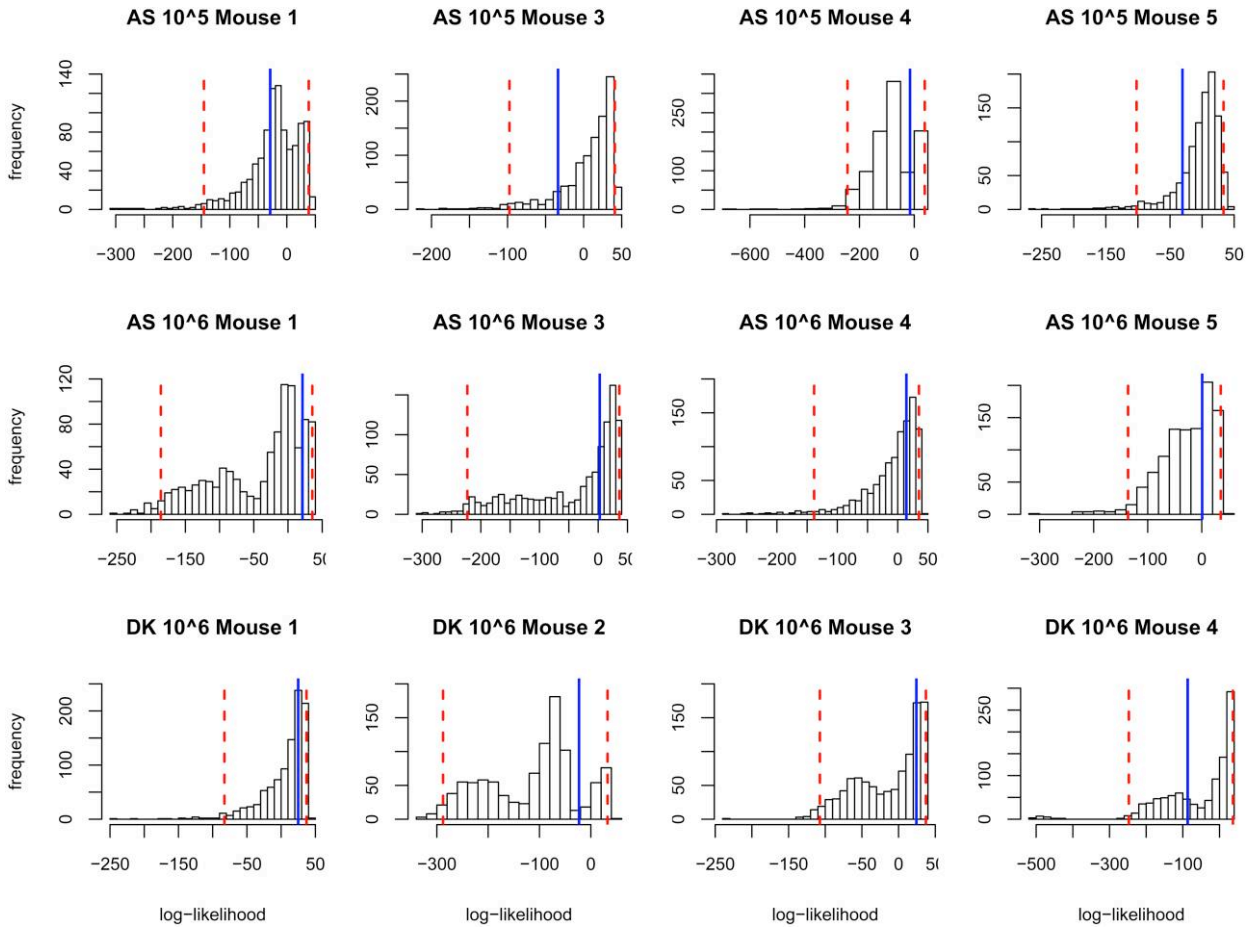

Figure C1: Expected distributions of L_{max}, the maximum log likelihood of the best-fit model given the data, for each individual mouse. These distributions are generated by calculating the log likelihood of the best-fit model and parameters given each of 1,000 artificial data sets. *Blue lines*, the observed L_{max} (log likelihood of best-fit model and parameters given the measured data). In each case, the blue line is within the 95% highest-density region of its expected distribution (*dashed red lines*); therefore, the model is a good fit for each data set.

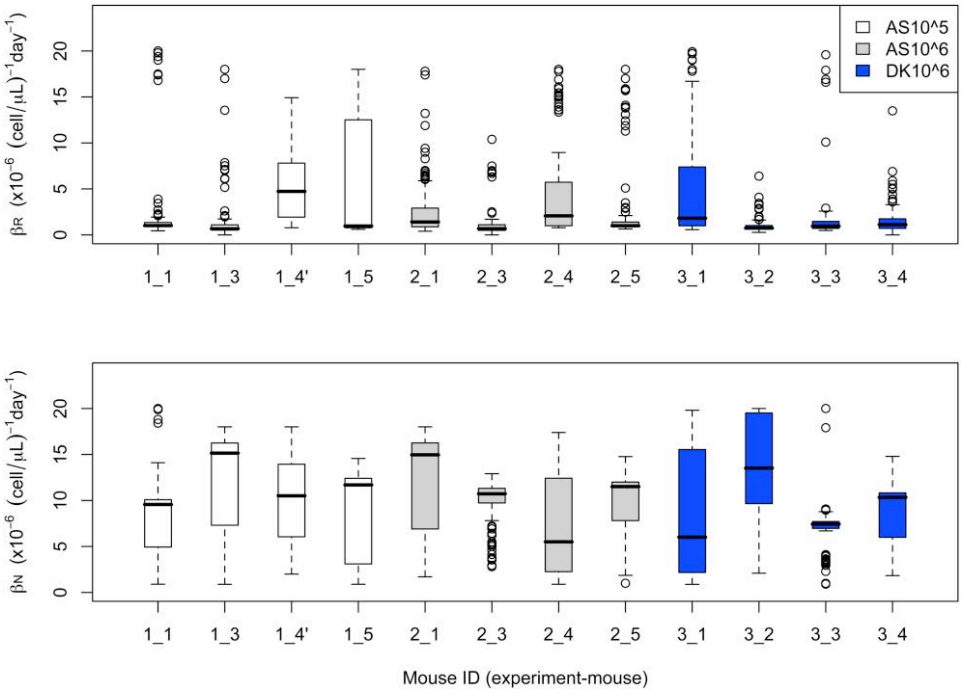

Figure C2: Boxplots of the estimated distributions of invasion rate for reticulocytes (*top*) and normocytes (*bottom*). Each boxplot contains 100 parameter estimates obtained from refitting simulated data sets (100 data sets per mouse). *Horizontal line*, median; *circles*, outliers; each box contains 50% of the values.

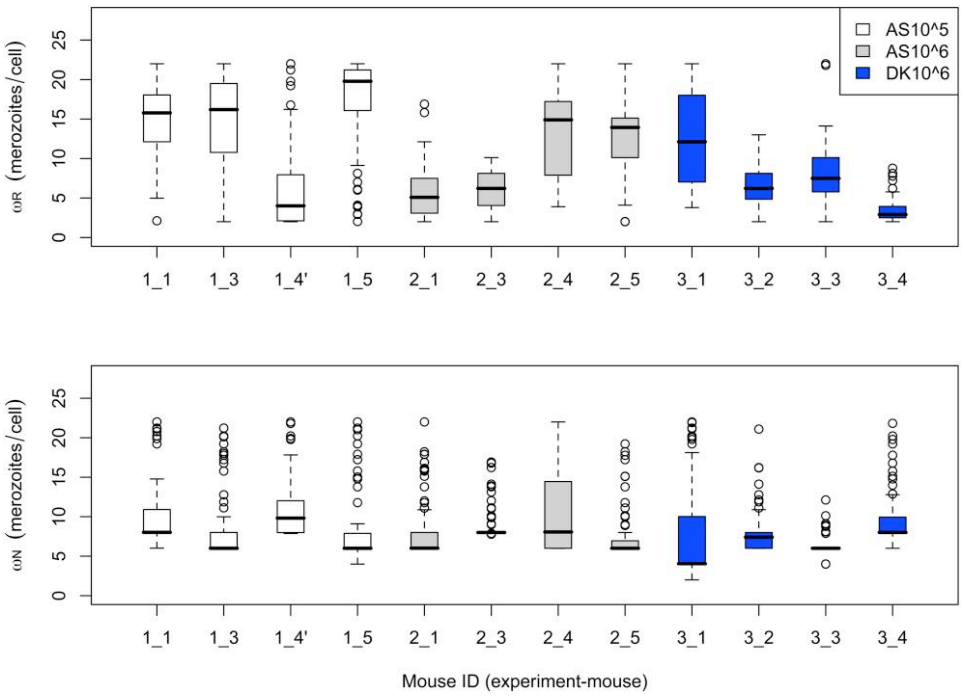

Figure C3: Boxplots of the estimated distributions of burst size for reticulocytes (*top*) and normocytes (*bottom*). Each boxplot contains 100 parameter

estimates obtained from refitting simulated data sets (100 data sets per mouse). *Horizontal line*, median; *circles*, outliers; each box contains 50% of the values.

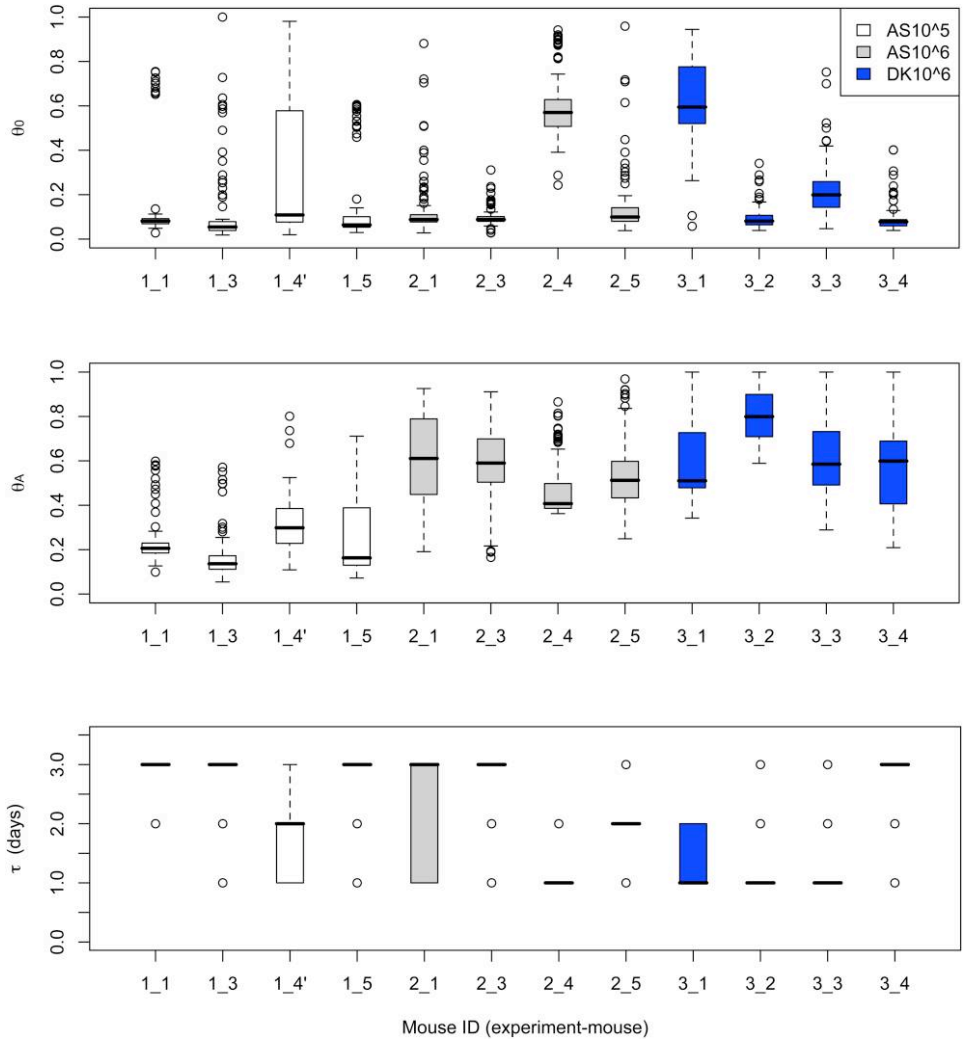

Figure C4: Boxplots of the estimated distributions of RBC production parameters: proportion of RBC deficit made up in one day under normal conditions (*top*), proportion of RBC deficit made up in one day under anemic conditions (*center*), and time lag due to maturation of RBC (*bottom*). Each boxplot contains 100 parameter estimates obtained from refitting simulated data sets (100 data sets per mouse). *Horizontal line*, median; *circles*, outliers; each box contains 50% of the values.

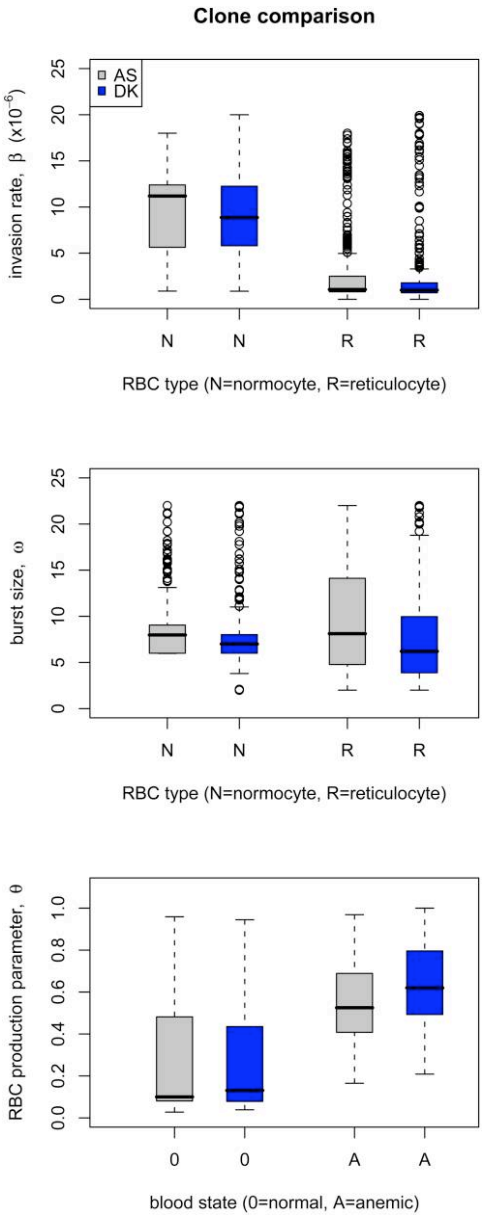

Figure C5: Boxplots of the combined estimated parameter distributions for the AS 106 (*gray*) and DK 106 (*blue*) experiments. Each boxplot contains 400 parameter estimates (100 data sets per mouse × 4 mice per strain). *Horizontal line*, median; *circles*, outliers; each box contains 50% of the values.

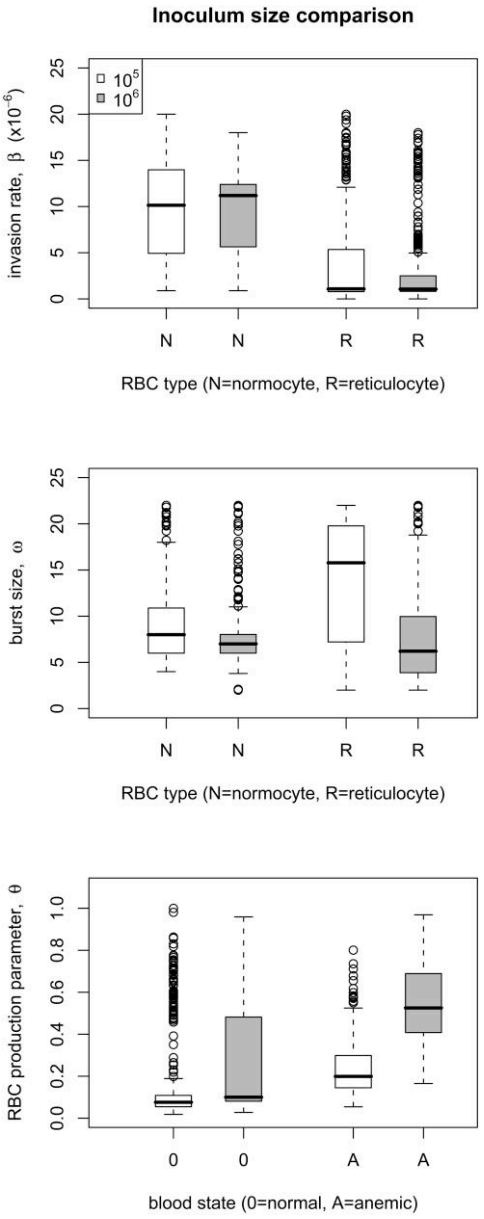

Figure C6: Boxplots of the combined estimated parameter distributions for the AS 105 (*white*) and AS106 (*gray*) experiments. Each boxplot contains 400 parameter estimates (100 data sets per mouse × 4 mice per dose). *Horizontal line*, median; *circles*, outliers; each box contains 50% of the values.

Literature Cited

Antia, R., A. Yates, and J. C. de Roode. 2008. The dynamics of acute malaria infections. I. Effect of the parasite's red blood cell preference. Proceedings of the Royal Society B: Biological Sciences 275: 1449–1458.

Bannerman, R. M. 1983. Hematology. Pages 293–312 *in* J. D. Small, H. L. Foster, and J. G. Fox, eds. The mouse in biomedical research. Academic Press, New York.

Barclay, V. C., L. Råberg, B. H. K. Chan, S. Brown, D. Gray, and A. F. Read. 2008. $CD4^+$ T cells do not mediate within-host competition between genetically diverse malaria parasites. Proceedings of the Royal Society B: Biological Sciences 275:1171–1179.

Beale, G. H., R. Carter, and D. Walliker. 1978. Genetics. Pages 213–245 *in* R. Killick-Kendrick and W. Peters, eds. Rodent malaria. Academic Press, London.

Bell, A. S., J. C. D. Roode, D. Sim, and A. F. Read. 2006. Within-host competition in genetically diverse malaria infections: parasite virulence and competitive success. Evolution 60:1358–1371.

Brown, K. N., and I. N. Brown. 1965. Immunity to malaria: antigenic variation in chronic infections of *Plasmodium knowlesi*. Nature 208:1286–1288.

Buckling, A., L. C. Ranford-Cartwright, A. Miles, and A. F. Read. 1999. Chloroquine increases *Plasmodium falciparum* gametocytogenesis in vitro. Parasitology 118:339–346.

Carter, R., and D. Walliker. 1975. New observations on malaria parasites of rodents of Central African Republic: *Plasmodium vinckei petteri* subsp. nov. and *Plasmodium chabaudi* Landau, 1965. Annals of Tropical Medicine and Parasitology 69:187–196.

Chang, K. H., M. Tam, and M. M. Stevenson. 2004. Modulation of the course and outcome of blood-stage malaria by erythropoietin-induced reticulocytosis. Journal of Infectious Diseases 189:735–743.

Cromer, D., K. J. Evans, L. Schofield, and M. P. Davenport. 2006. Preferential invasion of reticulocytes during late-stage *Plasmodium berghei* infection accounts for reduced circulating reticulocyte levels. International Journal for Parasitology 36:1389–1397.

de Roode, J. C., A. F. Read, B. H. K. Chan, and M. J. Mackinnon. 2003. Rodent malaria parasites suffer from the presence of conspecific clones in three-clone *Plasmodium chabaudi* infections. Parasitology 127:411–418.

de Roode, J. C., R. Culleton, S. J. Cheesman, R. Carter, and A. F. Read. 2004. Host heterogeneity is a determinant of competitive exclusion or coexistence in genetically diverse malaria infections. Proceedings of the Royal Society B: Biological Sciences 217:1073–1080.

de Roode, J. C., M. E. H. Helinski, M. A. Anwar, and A. F. Read. 2005*a*. Dynamics of multiple infection and within-host competition in genetically diverse malaria infections. American Naturalist 166:531–542.

de Roode, J. C., R. Pansini, S. J. Cheesman, M. E. H. Helinski, S. Huijben, A. R. Wargo, A. S. Bell, et al. 2005*b*. Virulence and competitive ability in genetically diverse malaria infections. Proceedings of the National Academy of Sciences of the USA 102:7624–7628.

Eichner, M., H. H. Diebner, L. Molineaux, W. E. Collins, G. M. Jeffery, and K. Dietz. 2001. Genesis, sequestration and survival of *Plasmodium falciparum* gametocytes: parameter estimates from fitting a model to malaria therapy data. Transactions of the Royal Society of Tropical Medicine and Hygiene 95:497–501.

Ganzoni, A., R. S. Hillman, and C. A. Finch. 1969. Maturation of the macroreticulocyte. British Journal of Haematology 16:119–134.

Garnham, P. C. C. 1966. Malaria parasites and other hæmosporidia. Blackwell Scientific, Oxford.

Good, M. F., and D. L. Doolan. 1999. Immune effector mechanisms in malaria. Current Opinion in Immunology 11:412–419.

Grimshaw, S. D., D. G. Whiting, and T. H. Morris. 2001. Likelihood ratio tests for a mixture of two von Mises distributions. Biometrics 57:260–265.

Haydon, D. T., L. Matthews, R. Timms, and N. Colegrave. 2003. Top-down or bottom-up regulation of intra-host blood-stage malaria: do malaria parasites most resemble the dynamics of prey or predator? Proceedings of the Royal Society B: Biological Sciences 270:289–298.

Hellriegel, B. 1992. Modeling the immune response to malaria with ecological concepts: short-term behavior against long-term equilibrium. Proceedings of the Royal Society B: Biological Sciences 250:249–256.

Hetzel, C., and R. M. Anderson. 1996. The within-host cellular dynamics of bloodstage malaria: theoretical and experimental studies. Parasitology 113:25–38.

Hilborn, R., and M. Mangel. 1997. The ecological detective: confronting models with data. Princeton University Press, Princeton, NJ.

Jakeman, G. N., A. Saul, W. L. Hogarth, and W. E. Collins. 1999. Anæmia of acute malaria infections in non-immune patients primarily results from destruction of uninfected erythrocytes. Parasitology 119:127–133.

Jarra, W., and K. N. Brown. 1989. Protective immunity to malaria: studies with cloned lines of rodent malaria in Cba. Parasite Immunology 11:1–13.

Johnson, J. B., and K. S. Omland. 2004. Model selection in ecology and evolution. Trends in Ecology & Evolution 19:101–108.

Killick-Kendrick, R., and W. Peters. 1978. Rodent malaria. Academic Press, London.

Langhorne, J., B. Simon-Haarhaus, and S. J. Meding. 1990. The role of $CD4^+$ T cells in the protective immune response to *Plasmodium chabaudi* in vivo. Immunology Letters 25:101–108.

Loeffler, M., K. Pantel, H. Wulff, and H. E. Wichmann. 1989. A mathematical model of erythropoiesis in mice and rats. I. Structure of the model. Cell and Tissue Kinetics 22:13–30.

Mackey, M. C. 1997. Mathematical models of hematopoietic cell replication and control. Pages 149–178 *in* H. G. Othmer, F. Adler, M. A. Lewis, and J. Dallon, eds. Case studies in mathematical modeling: ecology, physiology, and cell biology. Prentice Hall, Englewood Cliffs, NJ.

Mary, J. Y., A. J. Valleron, H. Croizat, and E. Frindel. 1980. Mathematical analysis of bone-marrow erythropoiesis: application to C3H mouse data. Blood Cells 6:241–254.

McAlister, R. O. 1977. Time-dependent loss of invasive ability of *Plasmodium berghei* merozoites in vitro. Journal of Parasitology 63:455–463.

McQueen, P. G., and F. E. McKenzie. 2004. Age-structured red blood cell susceptibility and the dynamics of malaria infections. Proceedings of the National Academy of Sciences of the USA 101: 9161–9166.

Molineaux, L., and K. Dietz. 1999. Review of intra-host models of malaria. Parasitologia 41:221–231.

Paul, R. E. L., F. Ariey, and V. Robert. 2003. The evolutionary ecology of *Plasmodium*. Ecology Letters 6:866–880.

Phillips, R. S., L. R. Brannan, P. Balmer, and P. Neuville. 1997. Antigenic variation during malaria infection: the contribution from the murine parasite *Plasmodium chabaudi*. Parasite Immunology 19:427–434.

Pombo, D. J., G. Lawrence, C. Hirunpetcharat, C. Rzepczyk, M. Bryden, N. Cloonan, K. Anderson, et al. 2002. Immunity to malaria after administration of ultra-low doses of red cells infected with *Plasmodium falciparum*. Lancet 360:610–617.

Råberg, L., J. C. de Roode, A. S. Bell, P. Stamou, D. Gray, and A. F. Read. 2006. The role of immune-mediated apparent competition in genetically diverse malaria infections. American Naturalist 168: 41–53.

Reece, S. E., A. B. Duncan, S. A. West, and A. F. Read. 2003. Sex ratios in the rodent malaria parasite, *Plasmodium chabaudi*. Parasitology 127:419–425.

———. 2005. Host cell preferences and variable transmission strategies in malaria parasites. Proceedings of the Royal Society B: Biological Sciences 272:511–517.

Shutler, D., S. E. Reece, A. Mullie, P. F. Billingsley, and A. F. Read. 2005. Rodent malaria parasites *Plasmodium chabaudi* and *P. vinckei* do not increase their rates of gametocytogenesis in response to

mosquito probing. Proceedings of the Royal Society B: Biological Sciences 272:2397–2402.

Stephens, R., and J. Langhorne. 2006. Priming of CD4(+) T cells and development of CD4(+) T cell memory: lessons for malaria. Parasite Immunology 28:25–30.

Stevenson, M. M., and E. M. Riley. 2004. Innate immunity to malaria. Nature Reviews Immunology 4:169–180.

Taylor, L. H., and A. F. Read. 1997. Why so few transmission stages? reproductive restraint by malaria parasites. Parasitology Today 13: 135–140.

Taylor-Robinson, A. W., and R. S. Phillips. 1994. Predominance of infected reticulocytes in the peripheral-blood of CD4(+) T-cell-depleted mice chronically infected with *Plasmodium chabaudi chabaudi*. Parasitology Research 80:614–619.

Timms, R., N. Colegrave, B. H. K. Chan, and A. F. Read. 2001. The effect of parasite dose on disease severity in the rodent malaria *Plasmodium chabaudi*. Parasitology 123:1–11.

Urban, B. C., R. Ing, and A. M. Stevenson. 2005. Early interactions between blood-stage *Plasmodium* parasites and the immune system. Current Topics in Microbiology and Immunology 297:25–70.

van Putten, L. M. 1958. The life span of red cells in the rat and the mouse as determined by labeling with Dfp32 in vivo. Blood 13: 789–794.

WHO and UNICEF. 2005. World malaria report 2005. http://rbm.who.int/wmr2005/index.html. Accessed November 2007.

Wiczling, P., and W. Krzyzanski. 2007. Method of determination of the reticulocyte age distribution from flow cytometry count by a structured-population model. Cytometry 71A:460–467.

Associate Editor: Jukka Jokela
Editor: Donald L. DeAngelis